Nonwetting droplet oscillation and displacement by viscoelastic fluids

Chiyu Xie [1,*] Ke Xu [2] Kishore Mohanty,[1] Moran Wang [3] and Matthew T. Balhoff[1,†]

[1]*Department of Petroleum and Geosystems Engineering, The University of Texas at Austin, Austin, Texas 78712, USA*
[2]*College of Engineering, Peking University, Beijing 100871, China*
[3]*Department of Engineering Mechanics and CNMM, Tsinghua University, Beijing 100084, China*

Many important applications in the food industry, biological systems, and recovery of fluids from the subsurface involve multiphase flow dynamics where one of the phases is a non-Newtonian, viscoelastic fluid. In this work, we investigate the role of viscoelastic displacing fluids in recovering trapped nonwetting fluids. We perform the lattice Boltzmann (LB) modeling of wetting viscoelastic fluids described by a Maxwell model that displace nonwetting, trapped droplets in three different pore geometries. Results show the oscillation of the trapped nonwetting droplets and subsequent release induced by the viscoelasticity of the displacing fluid. The oscillation behaviors are in qualitative agreement with recent experiments in microfluidic chips and micromodels. The disorder of streamlines in viscoelastic fluids is reported in the presence of another phase, which explains the observation of oscillations. In the geometry of a capillary tube that converges to a smaller constriction/throat, a vortex downstream of the droplet is found to prevent the droplet from entering the throat. In the geometry of a tube with an "x-shaped" solid grain, we find that the oscillation strength and extraction capability of displacing fluids monotonically increases with their elasticity. The results from the geometry of a tube with a "dead-end" branch show a linear relationship between the average mean vorticity and the square root of the Deborah number before the release of droplets.

I. INTRODUCTION

Viscoelastic fluids are non-Newtonian fluids that exhibit the properties of both viscous fluids and elastic solids [1]. Silly Putty and jelly are commonly used examples of viscoelastic fluids. Multiphase viscoelastic flow is of interest in many important fields such as the food industry [2] and biological systems [3,4]. An important property of viscoelastic fluids is that they have a memory of historical deformation. The complexity in rheology along with interfacial dynamics makes it difficult to fully predict the mechanisms of multiphase viscoelastic flow.

In subsurface engineering problems, such as the recovery of hydrocarbons, viscoelastic polymer solutions such as partially hydrolyzed polyacrylamide (HPAM) are commonly used in enhanced oil recovery (EOR) [5,6]. The primary purpose of these polymers is to improve mobility control (higher viscosity of displacing phase), but many studies have also shown reductions in residual, capillary-trapped oil. Experiments in porous rock cores performed by Wang *et al.* [7,8] showed the evidence that viscoelastic polymer can reduce residual oil after waterflood and subsequent Newtonian glycerol flood. Their micromodel studies [9–11] based on "dead-end" and other geometries

---

*Corresponding author: chiyu.xie@gmail.com
†Corresponding author: balhoff@mail.utexas.edu

provided more details showing the advantages of viscoelastic polymers for oil recovery at the microscale. By comparing the displacements using HPAM solutions with different concentrations, Xia *et al.* [12] further indicated the displacing efficiency of HPAM increases with its elasticity. From these observations, the authors hypothesized several mechanisms for the additional recovery of nonwetting fluid, such as the "pulling effect" (due to the tangential elastic force at the interfaces) and forming of the "oil thread" passages (continuous oil flow channels). Since HPAM solutions also exhibit other complex properties [13] such as the shear thinning behavior that makes its viscosity change with the shear rate, it is necessary to exclude these effects before any conclusions can be made regarding the effects of viscoelasticity on oil recovery. Urbissinova *et al.* [14] conducted core flooding experiments by using polyethylene oxide (PEO) solutions with similar shear viscosity, but different elasticities. The displacements by two different PEO solutions also showed that higher elasticity leads to lower residual oil saturation. However, the extra oil recovery by applying the polymer with a higher elasticity was not always observed when the oil viscosity is high [15] or at low-pressure-gradient flooding conditions [16]. Recently, a more interesting and surprising result was discovered by Erincik *et al.* [17]. By alternatively injecting high-elasticity and low-elasticity polymers into relatively homogeneous sandstones, they found that additional oil was continually produced. These discrepancies and new discoveries in core flooding experiments definitely require further investigations at the pore scale.

Clarke and co-workers [18,19] discovered oscillations of trapped oil droplets driven by the viscoelastic HPAM solution in a glass, porous micromodel. In contrast, no oscillation was found during the displacement by the inelastic xanthan polymer solution. In the single-phase micromodel study by Howe *et al.* [20], they observed unsteady streamlines during the flow of HPAM using particle tracking velocimetry (PTV). The authors suggested the term "elastic turbulence" [21–25] for these unique oscillation behaviors. They pointed out that the presence of elastic turbulence may help recover more oil by destabilizing trapped droplets. Qi [26] also reported the oscillations induced by viscoelastic polymers in a pore-throat (contraction-expansion) microchip. The nonwetting droplet driven by the viscoelastic polymer was prevented from passing through the narrow throat, even at much higher flow rates. Neither the oscillations nor the trapping was observed for displacing fluids that were purely viscous.

Recent developments in pore-scale simulation tools, such as the lattice Boltzmann (LB) method for non-Newtonian flow, offer a powerful way to model the aforementioned flows and observations [27–33]. Xie *et al.* [32] developed an LB framework for modeling multiphase flow of viscoelastic fluids by incorporating the Maxwell constitutive equation into a Rothman-Keller-type multiphase LB model [34–38] through an elastic forcing term. This model corrects the problem that leads to incorrect Maxwell fluid momentum equations encountered by previous LB models [39,40] for Maxwell viscoelastic fluid flows.

In this work, we focus on the pore-scale mechanisms of viscoelastic effects on oscillation and recovery of trapped nonwetting fluids. By applying the LB model proposed in Ref. [32], we are able to isolate the viscoelastic property of displacing fluids. In addition, we also provide a streamline analysis in the presence of another phase and compare it with the micromodel experiments. In Sec. II, numerical formulations of the multiphase viscoelastic LB scheme are briefly introduced. In Sec. III, three types of pore geometries are described as well as the computational details and definitions of the dimensionless numbers. In Sec. IV, we examine whether our model can capture the same oscillation phenomenon observed in Qi's thesis [26]. Then based on an "x-block" geometry and a dead-end geometry, we present more details and quantitative relationships on the role of viscoelastic oscillation in the extraction of the trapped nonwetting fluids. Finally, we draw conclusions in Sec. V.

II. NUMERICAL FORMULATIONS

This model applies N sets of LB equations to describe the motion of each fluid denoted by k. It uses a body force $\boldsymbol{F}_{\mathrm{el}}$ to account for the viscoelastic effects of Maxwell fluids. For each phase, the

LB equation is written as

$$f_i^k(\boldsymbol{x} + \boldsymbol{c_i}\Delta t, t + \Delta t) - f_i^k(\boldsymbol{x}, t) = \Omega_i^k\big[f_i^k(\boldsymbol{x}, t)\big] + \Gamma_i\left[\frac{\rho_k}{\rho}\boldsymbol{F}(\boldsymbol{x}, t)\right], \tag{1}$$

where f_i^k is the distribution function of fluid k on the ith velocity direction (the $D2Q9$ velocity space is used here); $\boldsymbol{x}$ is the lattice position, t is the time, Δt is the time step, $\boldsymbol{c_i}$ is the lattice velocity. ρ_k, ρ, and $\boldsymbol{u}$ are the macroscopic phase density, total density, and flow velocity, respectively. Ω_i^k is the collision operator combined by three suboperators $(\Omega_i^k)^S$, $(\Omega_i^k)^I$, and $(\Omega_i^k)^M$: $(\Omega_i^k)^S$ is the single-phase operator that governs the momentum evolution for each phase; $(\Omega_i^k)^I$ is the perturbation operator to account for the interfacial tension γ between phases; $(\Omega_i^k)^M$ is the recoloring operator to ensure mass conservation for each phase. The contour of phases is simply determined by the density field. The Γ_i in Eq. (1) is the forcing term [41] to account for the body force $\boldsymbol{F}$ consisting of gravity $\rho\boldsymbol{g}$ ($\boldsymbol{g}$ is the gravity acceleration) and the viscoelastic force $\boldsymbol{F}_{\mathrm{el}}$.

To obtain the viscoelastic force $\boldsymbol{F}_{\mathrm{el}}$, the Maxwell constitutive equation is adopted:

$$\dot{\boldsymbol{\varepsilon}} = \frac{\boldsymbol{\sigma}}{\eta_p} + \frac{\tau_{\mathrm{el}}}{\eta_p}\frac{d\boldsymbol{\sigma}}{dt}, \tag{2}$$

where $\dot{\varepsilon}$ is the strain rate, σ is the stress, η_p is the intrinsic polymer dynamic viscosity, and τ_{el} is the viscoelastic relaxation time. By integrating Eq. (2) over time from a finite value at $t = -\infty$, the stress can be expressed as

$$\boldsymbol{\sigma}(\boldsymbol{x}, t) = \frac{\eta_p}{\tau_{\mathrm{el}}} \int_{-\infty}^{t} \exp\left(-\frac{t - t'}{\tau_{\mathrm{el}}}\right)\dot{\boldsymbol{\varepsilon}}(\boldsymbol{x}, t')dt'. \tag{3}$$

Taking the divergence of the elastic stress, we have

$$\boldsymbol{F}_{\mathrm{el}}(\boldsymbol{x}, t) = \nabla \cdot \boldsymbol{\sigma} = \frac{\eta_p}{\tau_{\mathrm{el}}} \int_{-\infty}^{t} \exp\left(-\frac{t - t'}{\tau_{\mathrm{el}}}\right)\nabla^2\boldsymbol{u}(\boldsymbol{x}, t')dt'. \tag{4}$$

By assuming the numerical time step $\Delta t \ll \tau_{\mathrm{el}}$, this force can be further discretized by time step as

$$\boldsymbol{F}_{\mathrm{el}}(\boldsymbol{x}, t) = \left(1 - \frac{\Delta t}{\tau_{\mathrm{el}}}\right)\boldsymbol{F}_{\mathrm{el}}(\boldsymbol{x}, t - \Delta t) + \frac{\eta_p\Delta t}{\tau_{\mathrm{el}}}\nabla^2\boldsymbol{u}(\boldsymbol{x}, t - \Delta t). \tag{5}$$

Finally, by substituting Eq. (5) into Eq. (1) and by setting the "numerical kinematic viscosity" of viscoelastic fluid in the original LB scheme to approach zero, the LB equation (1) solves the correct momentum equation for Maxwell fluids in the single-phase region:

$$\partial_t \rho_k \boldsymbol{u} + (\boldsymbol{u} \cdot \nabla)\rho_k\boldsymbol{u} = -\nabla p + \boldsymbol{F}_{\mathrm{el}} + \rho\boldsymbol{g}. \tag{6}$$

By doing so, this method corrects the excess "LB viscous term" which remained in the early LB models for Maxwell fluid flows [39,40] that led to an incorrect Maxwell momentum equation. By selecting a much smaller numerical time step than the viscoelastic relaxation time τ_{el}, numerical instabilities induced by this treatment are avoided [32]. Most real fluids are better described by complex, nonlinear models, e.g., the finitely extensible nonlinear elastic (FENE) model and the Phan-Thien-Tanner (PTT) model. However, they are numerically challenging to solve and to our knowledge, have never been successfully applied to model multiphase flow in porous domains because of the difficulties in determining appropriate stress boundary conditions. Therefore, we choose to use this Maxwell-based multiphase LB framework to investigate the effect of elasticity on flow. More details of this model was presented in our previous work [32].

III. PROBLEM DEFINITION AND DIMENSIONLESS NUMBERS

To investigate the effect of viscoelasticity on the displacement of nonwetting fluids, we perform pore-scale simulations on three different geometries. The computational domains and initial phase
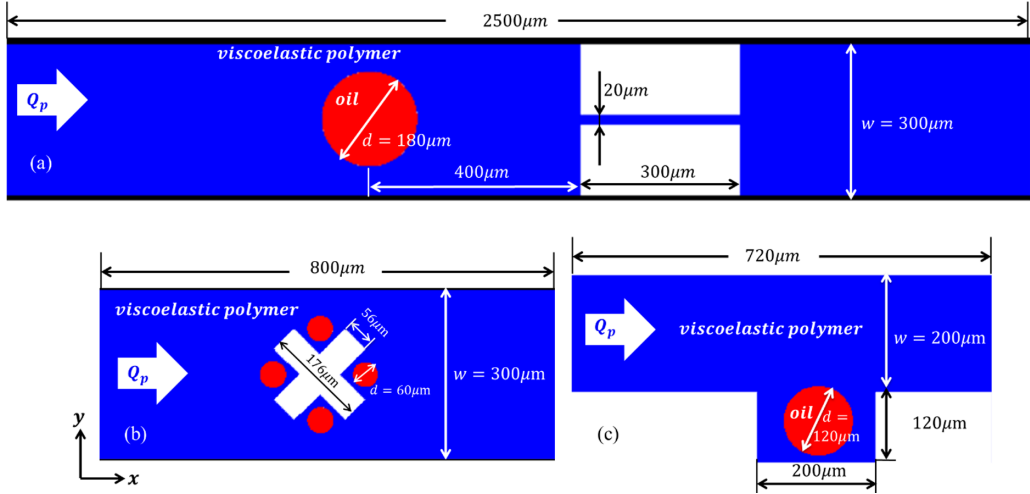
FIG. 1. Initial numerical configurations for three cases studied in this work: (a) a pore-throat structure; (b) an x-block structure, and (c) a dead-end pore structure.

distributions for each geometry are presented in Fig. 1, with red representing the nonwetting Newtonian oil droplets, blue representing the displacing fluid, and white being the solid or grain phase.

Figure 1(a) shows a pore-throat structure similar to the microfluidic chip in Qi's thesis [26]. The viscoelastic polymeric solution is injected into the pore containing a nonwetting oil droplet (shown in red). The modeling results of this case are compared with Qi's experiments [26], where the authors discovered that oil droplets driven by viscoelastic polymers with stronger elasticities were oscillating in the large pore and never entered the narrow throat even at high flow rates. This case is also desired as another validation for this numerical scheme, although it has been verified through various benchmarks such as capturing the unique bubble rising behaviors in a viscoelastic bulk fluid [32].

The flow domain in Fig. 1(b) contains an "x-shaped" solid grain at the centerline of the pore, with four nonwetting droplets of the same diameter initially trapped in the corners. This x-block geometry is similar to the unit in Clarke *et al.*'s micromodel [18]. Figure 1(c) presents a pore with a dead-end branch, where a nonwetting droplet is initially deposited in the mid-bottom of the dead-end pore. The discussions based on these two structures will reveal mechanisms of nonwetting drop mobilization by the viscoelastic fluid flow.

In all cases, the gravitational force is not accounted for as it is perpendicular to the xy plane. Velocity boundary conditions [42] are applied at the inlet with a constant flow rate Q_p. The convective outflow boundary conditions [43] are applied at the outlet to ensure smooth two-phase outflows. The upper and lower boundaries and other fluid-solid boundaries follow the bounce-back rule with completely bulk fluid wet conditions by assigning the wetting fluid concentration to be 1 on the solid wall [32].

Computational domains, fluid properties, and other parameters used for these simulations are listed in Table I. By taking the mean velocity at the inlet Q_p/w as the characteristic velocity, and by defining a characteristic length L (droplet diameter d for the pore-throat case, and the main pore width w for the other two cases), the main dimensionless numbers governing these processes are calculated as the Reynolds number, $\text{Re} = \rho_p Q_p L/(w \eta_p)$, the Capillary number, $\text{Ca} = \frac{\eta_p Q_p}{w \gamma}$, and the Deborah number, $\text{De} = \tau_{\text{el}} Q_p/(wL)$. Note that all the properties like density and dynamic viscosity are taken from the bulk displacing fluid. The selected parameters in Table I ensure small values of Re (< 0.1) and Ca ($< 1 \times 10^{-3}$), which are within the interest of many subsurface engineering

TABLE I. Parameters used for simulations.

Parameters	Pore-throat case	x-block case	Dead-end case
Domain size (lattices)	2500×300	400×150	360×160
Lattice space Δx (m)	1×10^{-6}	2×10^{-6}	2×10^{-6}
Time step Δt (s)	6.67×10^{-8}	1.67×10^{-7}	1.67×10^{-7}
Area flow rate Q_p (m^2/s)	4×10^{-7}	4×10^{-7}	4×10^{-7}
Density of the nonwetting fluid ρ_o (kg/m^3)	764	900	900
Viscosity of the nonwetting fluid η_o (Pa s)	0.0022	0.009	0.0045
Density of the viscoelastic displacing fluid $\rho_{p,\mathrm{el}}$ (kg/m^3)	1000	1000	1000
Viscosity of the viscoelastic displacing fluid $\eta_{p,\mathrm{el}}$ (Pa s)	0.032	0.01	0.01
Relaxation time of the viscoelastic displacing fluid τ_{el} (s)	0.069	0.01, 0.5	0.01 to 40
Density of the Newtonian displacing fluid $\rho_{p,N}$ (kg/m^3)	1000	1000	1000
Viscosity of the Newtonian displacing fluid $\eta_{p,N}$ (Pa s)	0.008	0.01	0.01
Interfacial tension γ (N/m)	0.04	0.04	0.04

problems [44]. The small Re and Ca also limit the strain of fluids, making it possible to use the Maxwell model in this work.

IV. RESULTS AND DISCUSSION

A. Pore-throat structure and viscoelastic oscillation

First, we attempt to qualitatively explain the observations of nonwetting droplet oscillation in a wetting, viscoelastic fluid as reported by Qi [26]. The rheological properties (relaxation time and viscosity) are chosen as the same as measured by Qi ($\tau_{\mathrm{el}} = 0.069$s, $\eta_{p,\mathrm{el}} = 0.032$ Pa s). The Deborah number for this case is De $= 0.51$. Our numerical configuration mimics the contraction-expansion microchip geometry in the experiment, but there are some important differences because of the 2D geometry implemented here. For example, (1) the pore-to-throat width ratio in the simulation is 300:20, which is equal to the pore-to-throat area ratio, but not the width ratio (300:60) in experiments; (2) in order to allow the flow of polymer between the droplet and walls in the two-dimensional (2D) simulation, the nonwetting droplet does not touch the wall, whereas the oil droplet is a squeezed ellipsoid touching the wall in the experiments due to the limit in the height direction.

Figure 2 compares the displacement of a nonwetting oil by a viscoelastic polymer with that by a Newtonian fluid; the arrows show the actual directions of droplet motion [see Supplemental Material [45] (Movies 1a and 1b) for the full time-dependent simulation]. Figure 3(a) records the change of distance from the drop center to the throat inlet in the x direction for both cases. A high-pass (20 Hz) fast Fourier transform is performed on the distance evolution curve of the viscoelastic case to better illustrate the droplet's motion, as shown in Fig. 3(b). These figures show the back-and-forth movement of the droplet in viscoelastic polymer predicted from simulations, while no oscillation is found for the Newtonian case and the droplet passes through the throat, which are all in agreement with Qi's experimental observations [26].

To explain the observations in the experiments and simulations, we investigate the flow fields by extracting snapshots of the streamlines, as shown in Fig. 4. The patterned vortices and symmetric streamlines are observed for the displacement by the Newtonian fluid, while for the displacement by the viscoelastic polymer, the flow is chaotic with disordered vortices and streamlines. Comparing the flow fields downstream of the droplet, a large vortex is observed in all viscoelastic simulations, which blocks the droplet. However, in the Newtonian case, no such vortex exists and streamlines provide a path towards the throat, which makes the droplet pass through at this flow rate.
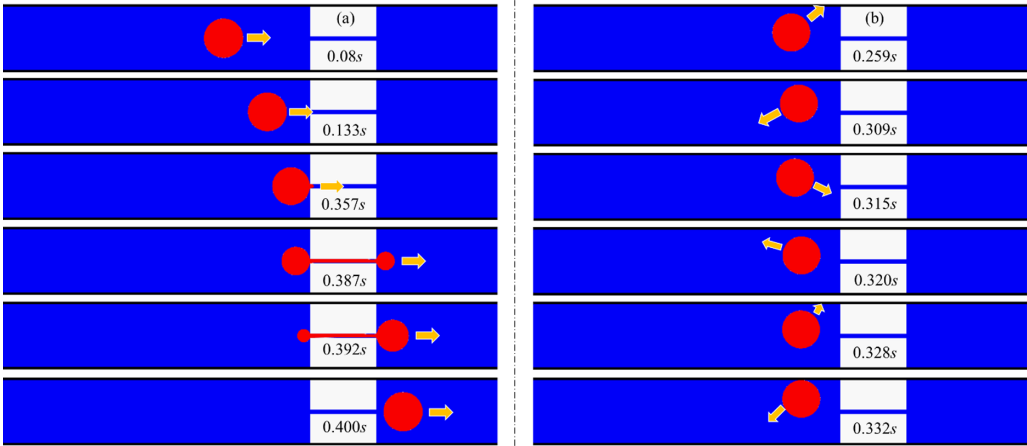
FIG. 2. Comparisons of oil displacements by (a) the Newtonian fluid and by (b) the viscoelastic polymer in the pore-throat geometry.

Figure 4(c) presents more details of the two big vortices beside the droplet. Their self-rotational times (the time required to rotate one radian) are estimated around 0.066 and 0.053 s, which are very close to the relaxation time of the viscoelastic fluid ($\tau_{el} = 0.069$ s). Therefore, it indicates that the chaotic streamline observed here is a kind of "elastic turbulence" [21–25]. The unique vortex and the oscillation behavior of a droplet displaced by a viscoelastic fluid are induced by the elastic memory of viscoelastic fluids, which are also similar to what causes the "cusp shape" and "negative wake" behind a bubble free rising in a viscoelastic fluid [46–49].

Here we present a simple explanation for the oscillation phenomenon under ideal conditions as illustrated in Fig. 5. Since the Reynolds number is quite small (0.0075 for the viscoelastic case), the driving force $\boldsymbol{F}_{drive}$ exerted on the oil droplet is mainly provided by the viscous force, $\boldsymbol{F}_{vis}$, which is assumed to be a constant as

$$F_{drive} \approx F_{vis} \propto \eta_p U_p d = \eta_p Q_p d / w, \tag{7}$$

while due to the viscoelastic fluid's memory effect, the magnitude of the elastic force $\boldsymbol{F}_{elastic}$ keeps changing with the droplet moving distance. Using the analogy of an elastic spring, it is assumed to
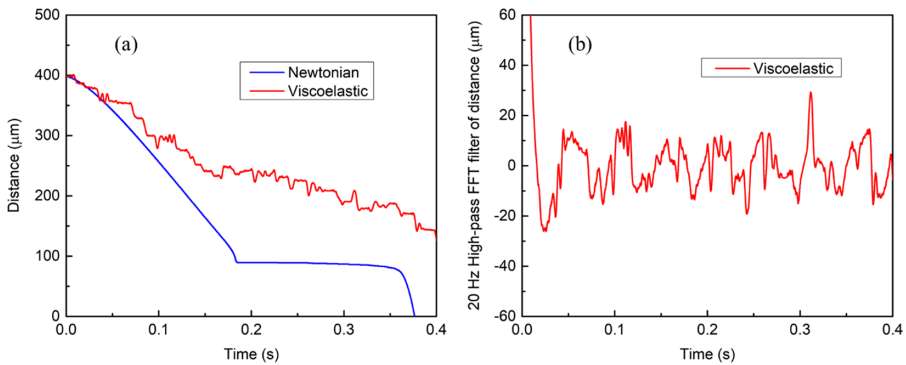

FIG. 3. (a) Evolution of the distance from drop center to the throat inlet in x direction for both cases. (b) A high-pass (20 Hz) fast Fourier transform performed on the distance evolution curve of the viscoelastic case.
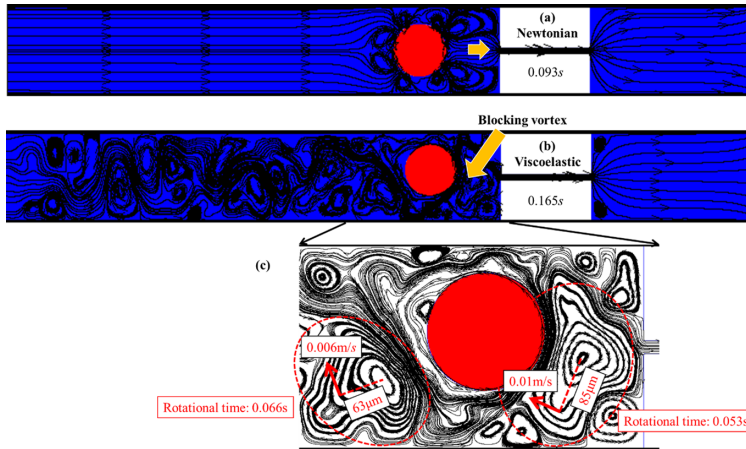
FIG. 4. Comparisons of streamlines extracted from typical snapshots during (a) the Newtonian fluid displacement and (b) the viscoelastic polymer displacement. (c) Local enlarged figure of (b) providing more details of the vortices.
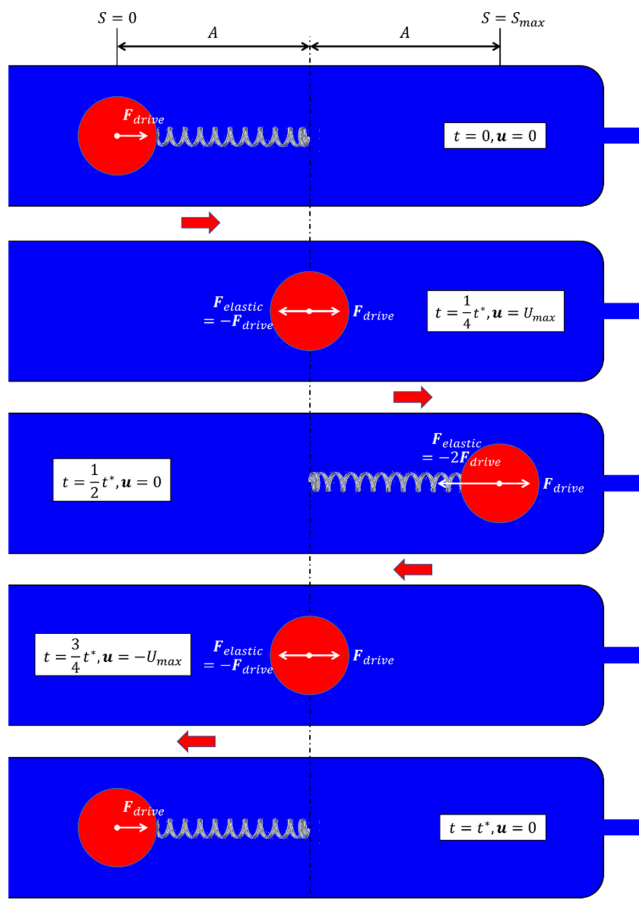

FIG. 5. An ideal sketch illustrating the oscillation behavior of a droplet driven by a viscoelastic fluid.

be linearly related to the displacement $S(t)$ as

$$F_{\text{elastic}}(t) \propto -dE \cdot S(t) = -d\eta_p \cdot S(t)/\tau_{\text{el}}, \tag{8}$$

where E is the elastic modulus of the viscoelastic polymer. Therefore, the motion of droplet approximately follows the simple harmonic motion with amplitude

$$A \propto F_{\text{drive}} \frac{\tau_{\text{el}}}{d\eta_p} = \frac{\tau_{\text{el}} Q_p}{w} = d\text{De}, \tag{9}$$

and time period

$$t^* = 2\pi \sqrt{\frac{m}{dE}} \propto d\sqrt{\frac{\rho_o \tau_{\text{el}}}{\eta_p}}, \tag{10}$$

where m denotes the droplet mass.

Initially ($t = 0$) the droplet starts from the status of $S(0) = 0$, $u(0) = 0$, and $F_{\text{elastic}}(0) = 0$, so the total force is F_{drive}, which will drive it forward. The droplet starts to accelerate and compress the polymer ahead. As long as the droplet keeps moving forward, the value of the opposite elastic force F_{elastic} will increase. When reaching $t = \frac{1}{4}t^*$, the elastic force $F_{\text{elastic}}(\frac{1}{4}t^*)$ is equal to $-F_{\text{drive}}$, indicating a zero total force, and the droplet reaches its maximum velocity U_{max} at the position $S(\frac{1}{2}t^*) = A$. During the period between $t = \frac{1}{4}t^*$ and $t = \frac{1}{2}t^*$, the droplet still moves forward, but with a decreasing velocity as the negative F_{elastic} keeps increasing. At time $t = \frac{1}{2}t^*$, the droplet velocity decreases to 0 and reaches its farthest position $S_{\text{max}} = 2A$ with the elastic force $F_{\text{elastic}}(\frac{1}{2}t^*) = -2F_{\text{drive}}$. The total force is then negative and $u(\frac{1}{2}t^*) = 0$; the droplet starts moving backward, and its position during $t = \frac{1}{2}t^*$ to $t = t^*$ follows the reverse process of the previous forward period. Finally the droplet returns to the initial status at $t = t^*$, and new cycles follow up periodically. This back-and-forth movement results in the appearance of the aforementioned vortex in Fig. 4(b). As a consequence, the droplet displaced by viscoelastic polymer will notably oscillate and be blocked in front of the throat.

It should be noted from Qi's experiment that the amplitude of oscillation increases with the flow rate while the frequency is independent of the flow rate. These two features are also predicted by the above simple theory according to Eqs. (9) and (10).

B. Release of nonwetting droplets from the x block by viscoelastic oscillation

From the above results of the pore-throat simulations, it seems that the viscoelastic oscillation prevents the nonwetting droplets from moving forward. But as mentioned in the Introduction, many experiments have shown that viscoelastic polymer recovered more oil than Newtonian displacing fluid with the same viscosity. Therefore, this section discusses whether the oscillations induced by the polymer's elasticity can help the displacement of nonwetting fluids.

Releasing of the trapped droplets by the x-block geometry shown in Fig. 1(b) is studied here. We compare two viscoelastic polymer solutions with different relaxation times: one with a larger value of $\tau_{\text{el}} = 0.5$ s and the other with a smaller value of $\tau_{\text{el}} = 0.01$ s. Another displacement by a Newtonian fluid with the same density and viscosity of the polymer is set as a reference case. The dimensionless numbers are then obtained as Re = 0.04 and Ca = 3.33 $\times 10^{-4}$. The Deborah numbers for these three cases are De = 2.22, De = 0.044, and De = 0, respectively.

Comparisons of droplet positions and streamlines are shown in Fig. 6 [see Supplemental Material [45] (Movies 2a, 2b, and 2c) for the entire processes]. In the Newtonian case, all four initially deposited oil droplets in the corners remain trapped due to the block by the "x" branches. In the low-elasticity polymer ($\tau_{\text{el}} = 0.01$ s and De = 0.044) cases, three droplets are stripped off except for the one droplet most upstream. However, in the high-elasticity polymer ($\tau_{\text{el}} = 0.5$ s and De = 2.22) cases, all the droplets are released from the solid x block. Some of the droplets released by the viscoelastic polymer contact each other and then coalesce into a bigger one. In terms of the
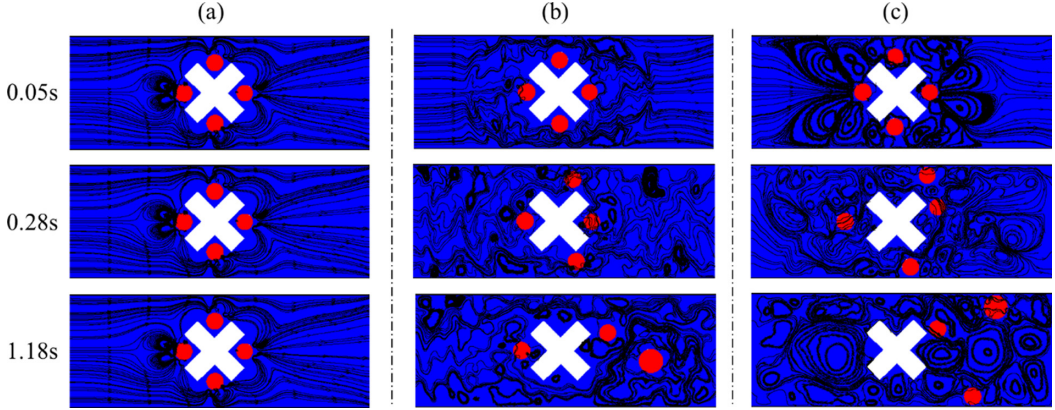
FIG. 6. Comparisons of the streamlines of oil displacement by (a) a Newtonian fluid, (b) a viscoelastic polymer with $\tau_{el} = 0.01$ s, and (c) a viscoelastic polymer with $\tau_{el} = 0.5$ s in the x-block geometry.

streamlines, a steady symmetrical pattern is maintained during displacement by the Newtonian fluid. However, the streamlines in two viscoelastic polymer displacing cases are disordered and unsteady. As the Reynolds number is quite small here, this turbulence is caused only by the viscoelastic oscillation. To quantify the strength of oscillations, we further calculate the magnitude of vorticity through

$$|\boldsymbol{\omega}| = \left| \frac{\partial u_y}{\partial x} - \frac{\partial u_x}{\partial y} \right|, \tag{11}$$

with its nondimensional form being $\tilde{\omega} = wL|\boldsymbol{\omega}|/Q_p$.

Figure 7 presents the evolution of the vorticity fields in these simulations. The mean vorticity magnitude of the Newtonian displacing fluid is $66.60 \, \text{s}^{-1}$, and remains constant with time. The mean vorticity magnitudes of the viscoelastic polymers are higher than that of the Newtonian fluid and vary with time due to the movement of droplets. And at the same moment, the vorticity magnitude of the high-elasticity polymer is always larger than that of the low-elasticity polymer, which indicates a stronger oscillation.

Combining the results from Figs. 6 and 7, we demonstrate that the oscillation in the flow field induced by the viscoelastic memory effect can help the release of trapped nonwetting droplets from
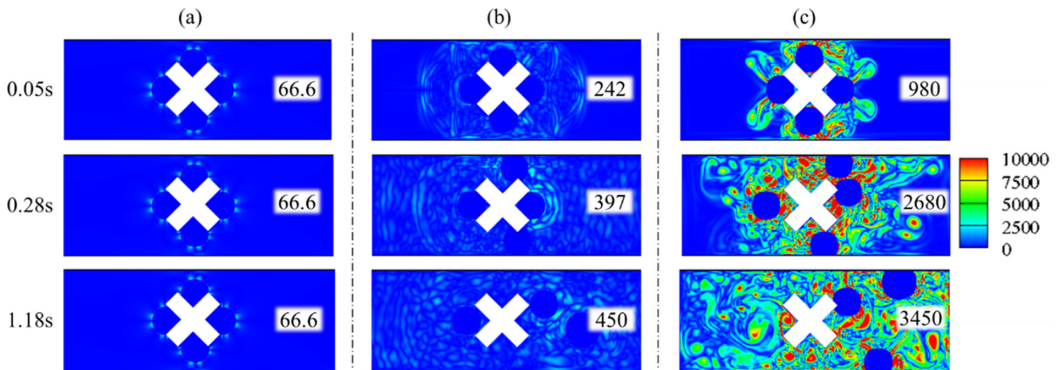

FIG. 7. Evolution of the vorticity fields in (a) the Newtonian fluid, (b) the viscoelastic polymer with $\tau_{el} = 0.01$ s, and (c) the viscoelastic polymer with $\tau_{el} = 0.5$ s during displacements in the x-block geometry.
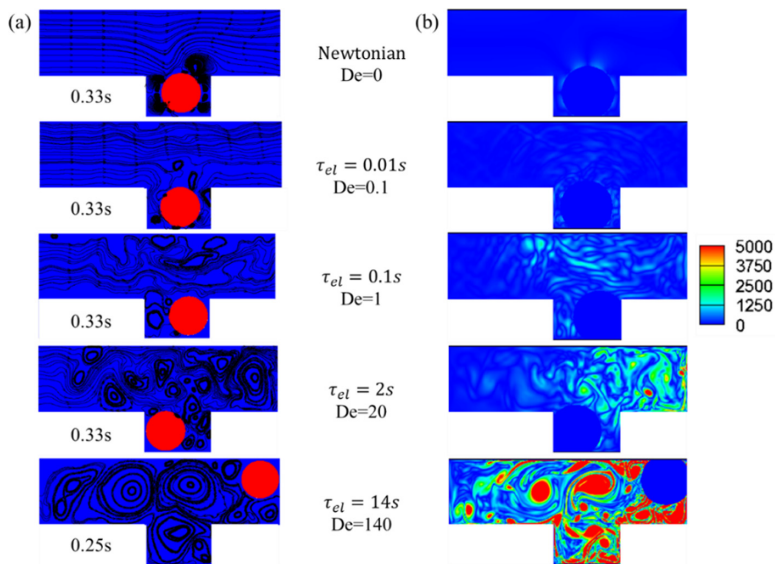
FIG. 8. Snapshots of (a) the streamlines and (b) the vorticity fields during displacements in the dead-end geometry by different fluids.

their initially trapped positions. The strength of the oscillation and the ability to release the droplets increase with the polymer's elasticity (indicated by De).

C. Release of a nonwetting droplet trapped in a dead-end pore by viscoelastic oscillation

Naturally occurring porous media have many dead-end pores and nonwetting phase droplets often get trapped in such pores. To find a quantitative relationship between the oscillation strength ($|\boldsymbol{\omega}|$) and the polymer's elasticity (De), we perform simulations based on the dead-end geometry shown in Fig. 1(c). In this section, nine viscoelastic polymer solutions with relaxation times from 0.01 to 40 s are considered, resulting in Deborah numbers varying from 0 to 400. The Reynolds number and the Capillary number are Re = 0.04 and Ca = 5 $\times$ 10^{-4}, respectively. A Newtonian reference case is also presented.

Snapshots of the streamlines and the vorticity fields during the displacements by five different fluids are shown in Figs. 8(a) and 8(b) [see Supplemental Material [45] (Movies 3a–3e) for the full time-dependent numerical simulation]. Similar to the previous results shown in the x-block cases, the disorder in streamlines and the vorticity magnitude increase with the Deborah number. For the Newtonian case, the streamlines in the main pore region are nearly straight. For the polymer with extremely weak elasticity ($\tau_{\mathrm{el}} = 0.01$ s and De = 0.1), the pattern of streamlines are close to those in the Newtonian case. Therefore, among these five cases, only the polymer with the largest elasticity ($\tau_{\mathrm{el}} = 14$ s and De = 140) successfully extracts the droplet from the dead-end pore by its strong oscillation.

We also compute the evolution of the mean vorticity magnitude in displacing fluids for each case, as illustrated in Fig. 9. These curves further indicate the increasing trend of the oscillation strength ($|\boldsymbol{\omega}|$) with the polymer's elasticity. There are three polymers with larger elasticities that extract the droplets, while in other cases the droplets are still trapped. During the short initial stage, the vorticity fields in all cases increase as the downstream fluids start to flow. Then the mean vorticity curves gradually go down for the trapped cases, since the fixed positions of droplets make the flow fields evolve towards a steady state. However, for the three extracted cases, notable jumps are observed which denote the initiation of the droplet extraction. The critical mean vorticity is about 2200 s^{-1} to
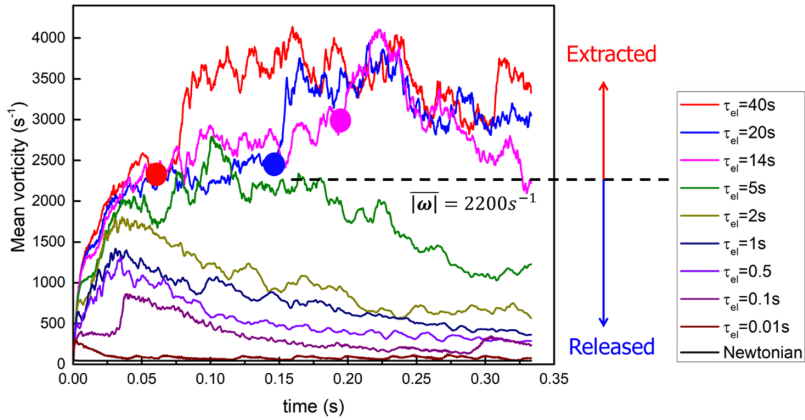
FIG. 9. Evolution of the mean vorticity magnitude in displacing fluids (the solid points denote the initial moments of the droplet extraction).

release droplets. After the transition moments, the vorticity fields in these cases remain at high levels as the extracted droplets continue to oscillate in the main pore before moving out of the boundary. It is also found that the larger the polymer's elasticity, the earlier the extraction begins.

The average values of the mean vorticity curves in Fig. 9 over the simulation time are nondimensionalized by the reciprocal of the characteristic time Q_p/wL and plotted with $\sqrt{\text{De}}$, as presented in Fig. 10. Based on the monotonically increasing relationship between the oscillation strength and the Deborah number, Fig. 10 can be divided into two regions by a critical Deborah number—smaller than that which denotes the trapped region and the other is the extracted region. It is difficult to find an evident quantitative relationship between the nondimensional average mean vorticity ($\tilde{\omega}$) and De in the extracted region because the two-phase configurations change rapidly. While in the trapped region, the droplets stay in the dead-end pore with comparable phase configurations. It seems a linear correlation between $\tilde{\omega}$ and $\sqrt{\text{De}}$ works here, however, a more fundamental explanation is expected.

The exact linear correlation and the critical Deborah number found in Fig. 10 should be determined by factors like droplet diameter, size of the dead-end pore, etc. As shown in Fig. 11, we further discuss the impact of the dead-end size on droplet extraction by changing the depth from
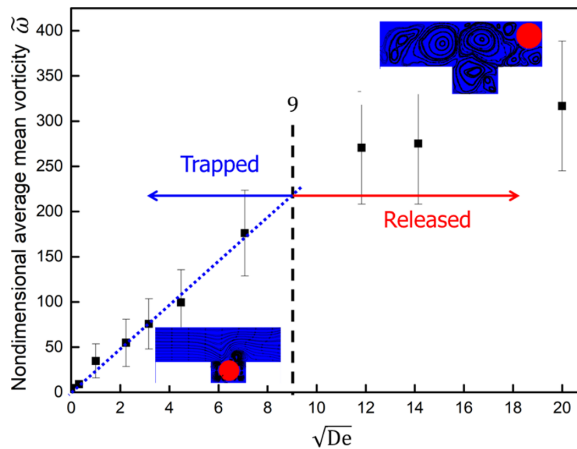

FIG. 10. Correlation between the nondimensional average mean vorticity magnitude over time and $\sqrt{\text{De}}$.
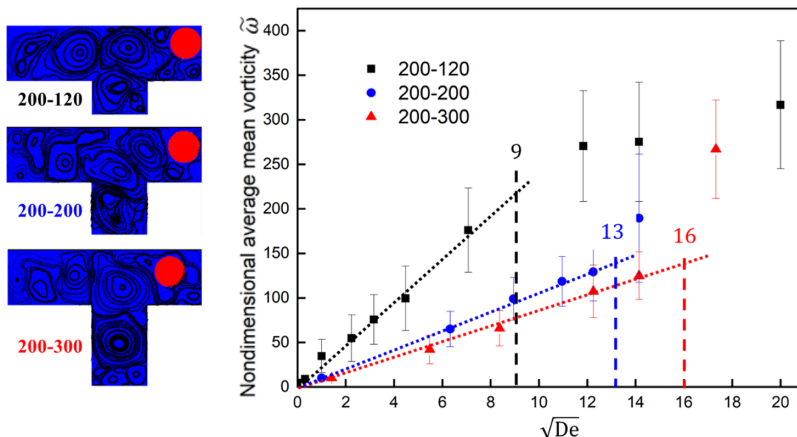
FIG. 11. The impact of the dead-end depth on droplet extraction.

120 to 300 μm. The width of the main pore is kept as 200 μm. We find that the critical Deborah numbers are around 9, 13, and 16, respectively, which increase with the depth of the dead-end pore. This is expected since a deeper dead-end pore indicates a more difficult condition to release the droplet.

Comparing with the x-block case, the critical Deborah number required to release the trapped droplet in the dead-end pore is much larger. This is mainly due to the difference in the complexity of the geometries, as the more complex x-block geometry itself is able to provide additional disturbance to oscillate the droplets. Therefore, the droplets in the x-block geometry are more easily extracted and a smaller Deborah number is sufficient.

V. CONCLUSIONS

A recently developed lattice Boltzmann model for multiphase viscoelastic flows has been applied to explore the effects of viscoelasticity on nonwetting droplet mobilization. Flow and droplet mobilization in three different pore geometries are simulated. In contrast to most published microfluidic experiments, the viscoelastic property of displacing fluids is isolated from other non-Newtonian effects such as shear thinning and shear thickening. The oscillation induced by the viscoelastic memory effect is considered to be the main reason for the enhanced recovery of nonwetting fluids by using viscoelastic displacing fluids. The disorder of streamlines in viscoelastic fluids is reported in the presence of another fluid phase.

In the "pore-throat" geometry, the simulation results qualitatively agree with experiments by Qi [26]; the nonwetting droplet driven by the high-elasticity polymers oscillates and does not pass through the narrow throat even at high flow rates. We observe the existence of a large vortex downstream of the droplet in the viscoelastic case by our simulation, which should be the direct reason for blocking the droplet. A derivation based on the theory of simple harmonic motion further explains the periodic oscillation behavior of the droplet. Although it appears that such oscillation prevents the nonwetting droplets moving forward in main pores, the x-block and dead-end cases demonstrate that such viscoelastic oscillation can result in the mobilization of nonwetting fluids from trapped positions. Moreover, by analyzing the vorticity fields, the oscillation strength and the extraction capability of displacing fluids are found to monotonically increase with their elasticity. Prior to the mobilization, a linear correlation between the average mean vorticity and $\sqrt{\text{De}}$ is obtained for the dead-end case. Combining these results together may provide an explanation to the surprising reduction of residual oil by alternative injection of high-elasticity and low-elasticity polymers found by Erincik *et al.* [17]. The high-elasticity polymer helps to release droplets from
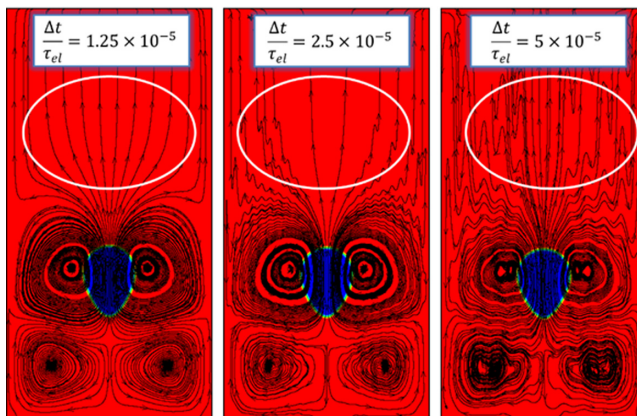
FIG. 12. The effect of simulation time step on the streamlines during a Newtonian bubble rising in a viscoelastic fluid [32]. The Capillary number Ca and the Deborah number De are 21.2 and 4, respectively.

trapped positions, but some of the extracted droplets oscillate in big pores; subsequently injected low-elasticity polymers help push these droplets out, but may lead to trapped droplets in new positions. Therefore, such rearrangements of fluid distribution inside the porous rock continues to reduce residual oil.

We only focus on nonwetting droplets here, however, future studies on the effect of wettability and by using more complex nonlinear constitutive equations are expected. The linear correlation between the average vorticity and the square root of De also deserves a further fundamental investigation.

APPENDIX: DISCUSSION OF THE CHAOTIC STREAMLINES

Here we are to prove that the disorder of streamlines we observe is not a result of numerical artifacts. We had a benchmark test in our previous paper [32] on the droplet rising problem and

TABLE II. Simulation parameters used for convergence tests.

| Simulation parameters		Pore-throat case $\tau_{el} = 0.069$ s	x-block case $\tau_{el} = 0.5$ s	Dead-end case $\tau_{el} = 14$ s
Base grids	Domain size (lattices)	1550×300	400×150	360×160
	Lattice space Δx (m)	1×10^{-6}	2×10^{-6}	2×10^{-6}
	Time step Δt (s)	6.67×10^{-8}	1.67×10^{-7}	1.67×10^{-7}
Double grids	Domain size (lattices)	3100×600	800×300	720×320
	Lattice space Δx (m)	0.5×10^{-6}	1×10^{-6}	1×10^{-6}
	Time step Δt (s)	1.67×10^{-8}	4.17×10^{-8}	4.17×10^{-8}
Half grids	Domain size (lattices)	775×150	200×75	180×80
	Lattice space Δx (m)	2×10^{-6}	4×10^{-6}	4×10^{-6}
	Time step Δt (s)	6.67×10^{-8}	1.67×10^{-7}	1.67×10^{-7}
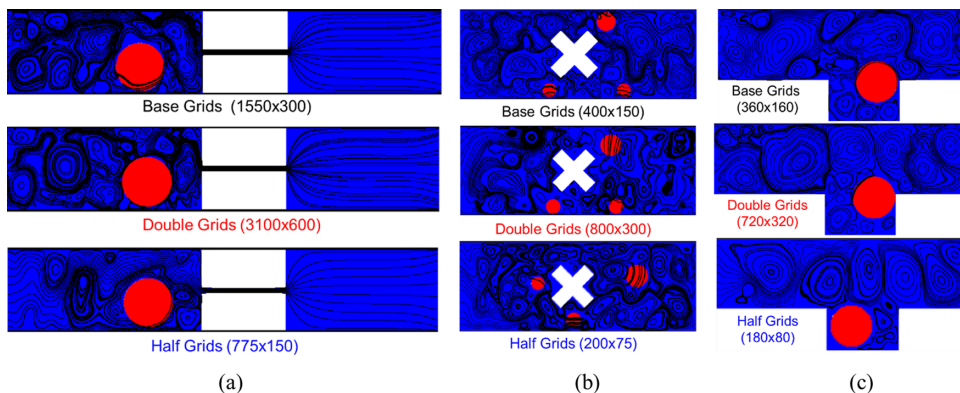
FIG. 13. Convergence tests for the droplet displacement by viscoelastic fluids in (a) the pore-throat channel, (b) the x-block channel, and (c) the dead-end channel.

showed a real kind of numerical instability caused by using larger time steps than the relaxation time. Fig. 12 shows the effect of the simulation time step on the streamlines during a Newtonian bubble rising in a viscoelastic fluid. All of these cases capture the negative wake and cusp shape, which are caused by the viscoelastic effect [46–49]. However, numerical instabilities (the local disorders observed in the white circled area) increase with time step. For the case with the smallest time step, the upper streamlines are steady and smooth, which indicates no numerical instabilities. As a result, a criterion for the time step ($\Delta t < 1.25 \times 10^{-5} \tau_{\mathrm{el}}$) was set in [32]. Note that the time steps for all the cases in this paper satisfy this criterion and the domain sizes are comparable with the droplet rising case (200×400) we studied. In particular, the straight streamlines (e.g., the downstream streamlines in the pore-throat case) are smooth and do not have such kind of numerical instabilities. Therefore, the disorder of streamlines we report in this paper is not a result of the time-step caused numerical artifact.

We further implement convergence tests for the droplet displacement by viscoelastic fluids in all the three pore geometries. The results obtained by using double grids and half grids are compared with the results shown in the main text. All the physical parameters are kept the same, except the domain size, the lattice space, and the time step listed in Table II.

Figure 13 presents the comparisons of streamlines and droplet positions during displacements obtained by different simulation grids for each case. All of the simulations using different resolutions capture the main chaotic streamlines without the local small disorders, and a finer resolution seems to capture more chaotic structures, particularly in the pore-throat case. Although there are certain differences in the streamlines, in general, the base-grid results are similar to the double-grid results. For the sake of computational cost, we use the base grids for the results shown in the main content.

Therefore, all of the above results indicate that the chaotic streamlines we got in this paper are due to the physical viscoelastic effects and not due to numerical instabilities.

[1] M. M. Denn, Issues in viscoelastic fluid mechanics, Annu. Rev. Fluid Mech. **22**, 13 (1990).

[2] M. A. Rao, Rheology of food gum and starch dispersions, in *Rheology of Fluid and Semisolid Foods: Principles and Applications*, edited by G. V. Barbosa-Canovas (Springer, Boston, 2007), pp. 153–222.

[3] N. Bessonov, A. Sequeira, S. Simakov, Y. Vassilevskii, and V. Volpert, Methods of blood flow modelling, Math. Modell. Nat. Phenom. **11**, 1 (2016).

[4] M. Brust, C. Schaefer, R. Doerr, L. Pan, M. Garcia, P. E. Arratia, and C. Wagner, Rheology of Human Blood Plasma: Viscoelastic Versus Newtonian Behavior, Phys. Rev. Lett. **110**, 078305 (2013).

[5] K. S. Sorbie, *Polymer-Improved Oil Recovery* (Springer, New York, 2013).

[6] K. C. Taylor and H. A. Nasr-El-Din, Water-soluble hydrophobically associating polymers for improved oil recovery: a literature review, J. Petrol. Sci. Eng. **19**, 265 (1998).

[7] D. Wang, G. Wang, W. Wu, H. Xia, and H. Yin, The influence of viscoelasticity on displacement efficiency–from micro to macro scale, SPE Annual Technical Conference and Exhibition, 11-14 November 2007, Anaheim, California, https://www.onepetro.org/conference-paper/SPE-109016-MS.

[8] D. Wang, J. Cheng, Q. Yang, G. Wenchao, L. Qun, and F. Chen, Viscous-elastic polymer can increase microscale displacement efficiency in cores, SPE Annual Technical Conference and Exhibition, 1-4 October 2000, Dallas, Texas, https://www.onepetro.org/conference-paper/SPE-63227-MS.

[9] D. Wang, J. Cheng, H. Xia, Q. Li, and J. Shi, Viscous-elastic fluids can mobilize oil remaining after water-flood by force parallel to the oil-water interface, SPE Asia Pacific Improved Oil Recovery Conference, 6-9 October 2001, Kuala Lumpur, Malaysia, https://www.onepetro.org/conference-paper/SPE-72123-MS.

[10] D. Wang, H. Xia, Z. Liu, and Q. Yang, Study of the mechanism of polymer solution with visco-elastic behavior increasing microscopic oil displacement efficiency and the forming of steady "oil thread" flow channels, SPE Asia Pacific Oil and Gas Conference and Exhibition, 17-19 April 2001, Jakarta, Indonesia, https://www.onepetro.org/conference-paper/SPE-68723-MS.

[11] H. Xia, Y. Ju, F. Kong, and J. Wu, Effect of elastic behavior of hpam solutions on displacement efficiency under mixed wettability conditions, SPE Annual Technical Conference and Exhibition, 26-29 September 2004, Houston, Texas, https://www.onepetro.org/conference-paper/SPE-90234-MS.

[12] H. Xia, D. Wang, G. Wang, and J. Wu, Effect of polymer solution viscoelasticity on residual oil, Pet. Sci. Technol. **26**, 398 (2008).

[13] D. A. Z. Wever, F. Picchioni, and A. A. Broekhuis, Polymers for enhanced oil recovery: a paradigm for structure–property relationship in aqueous solution, Prog. Polym. Sci. **36**, 1558 (2011).

[14] T. Urbissinova, J. J. Trivedi, and E. Kuru, Effect of elasticity during viscoelastic polymer flooding-a possible mechanism of increasing the sweep efficiency, SPE Western Regional Meeting, 27-29 May 2010, Anaheim, California, https://www.onepetro.org/conference-paper/SPE-133471-MS.

[15] E. C. M. Vermolen, M. J. T. Van Haasterecht, and S. K. Masalmeh, A systematic study of the polymer visco-elastic effect on residual oil saturation by core flooding, SPE EOR Conference at Oil and Gas West Asia, 31 March-2 April 2014, Muscat, Oman, https://www.onepetro.org/conference-paper/SPE-169681-MS.

[16] P. Qi, D. H. Ehrenfried, H. Koh, and M. T. Balhoff, Reduction of residual oil saturation in sandstone cores by use of viscoelastic polymers, SPE J. (Soc. Pet. Eng.) **22**, 447 (2017).

[17] M. Z. Erincik, P. Qi, M. T. Balhoff, and G. A. Pope, New method to reduce residual oil saturation by polymer flooding, SPE Annual Technical Conference and Exhibition, 9-11 October 2018, San Antonio, Texas, https://www.onepetro.org/conference-paper/SPE-187230-MS.

[18] A. Clarke, A. M. Howe, J. Mitchell, J. Staniland, and L. A. Hawkes, How viscoelastic-polymer flooding enhances displacement efficiency, SPE J. (Soc. Pet. Eng.) **21**, 675 (2016).

[19] J. Mitchell, K. Lyons, A. M. Howe, and A. Clarke, Viscoelastic polymer flows and elastic turbulence in three-dimensional porous structures, Soft Matter **12**, 460 (2016).

[20] A. M. Howe, A. Clarke, and D. Giernalczyk, Flow of concentrated viscoelastic polymer solutions in porous media: effect of mw and concentration on elastic turbulence onset in various geometries, Soft Matter **11**, 6419 (2015).

[21] R. G. Larson, E. S. G. Shaqfeh, and S. J. Muller, A purely elastic instability in taylor–couette flow, J. Fluid Mech. **218**, 573 (1990).

[22] P. Pakdel and G. H. McKinley, Elastic Instability and Curved Streamlines, Phys. Rev. Lett. **77**, 2459 (1996).

[23] G. H. McKinley, P. Pakdel, and A. Öztekin, Rheological and geometric scaling of purely elastic flow instabilities, J. Non-Newtonian Fluid Mech. **67**, 19 (1996).

[24] A. Groisman and V. Steinberg, Elastic turbulence in a polymer solution flow, Nature (London) **405**, 53 (2000).

[25] A. Groisman and V. Steinberg, Elastic turbulence in curvilinear flows of polymer solutions, New J. Phys. **6**, 29 (2004).

[26] P. Qi, The effect of polymer viscoelasticity on residual oil saturation, Ph.D. thesis, The University of Texas at Austin, 2018.

[27] T. N. Phillips and G. W. Roberts, Lattice boltzmann models for non-newtonian flows, IMA J. Appl. Math. 76, 790 (2011).

[28] J. Su, J. Ouyang, X. Wang, and B. Yang, Lattice boltzmann method coupled with the oldroyd-b constitutive model for a viscoelastic fluid, Phys. Rev. E 88, 053304 (2013).

[29] S. Zou, X. Xu, J. Chen, X. Guo, and Q. Wang, Benchmark numerical simulations of viscoelastic fluid flows with an efficient integrated lattice boltzmann and finite volume scheme, Adv. Mech. Eng. 7, 805484 (2014).

[30] C. Xie, J. Zhang, V. Bertola, and M. Wang, Lattice boltzmann modeling for multiphase viscoplastic fluid flow, J. Non-Newtonian Fluid Mech. 234, 118 (2016).

[31] C. Xie, W. Lv, and M. Wang, Shear-thinning or shear-thickening fluid for better eor? — a direct pore-scale study, J. Pet. Sci. Eng. 161, 683 (2018).

[32] C. Xie, W. Lei, and M. Wang, Lattice boltzmann model for three-phase viscoelastic fluid flow, Phys. Rev. E 97, 023312 (2018).

[33] N. Wang, H. Liu, and C. Zhang, Deformation and breakup of a confined droplet in shear flows with power-law rheology, J. Rheol. 61, 741 (2017).

[34] S. Leclaire, M. Reggio, and J. Trépanier, Numerical evaluation of two recoloring operators for an immiscible two-phase flow lattice boltzmann model, Appl. Math. Models 36, 2237 (2012).

[35] S. Leclaire, M. Reggio, and J. Trépanier, Progress and investigation on lattice boltzmann modeling of multiple immiscible fluids or components with variable density and viscosity ratios, J. Comput. Phys. 246, 318 (2013).

[36] S. Leclaire, N. Pellerin, M. Reggio, and J. Trépanier, Enhanced equilibrium distribution functions for simulating immiscible multiphase flows with variable density ratios in a class of lattice boltzmann models, Int. J. Multiphase Flow 57, 159 (2013).

[37] S. Leclaire and N. Pellerin, Unsteady immiscible multiphase flow validation of a multiple-relaxation-time lattice boltzmann method, J. Phys. A: Math. Theor. 47, 105501 (2014).

[38] S. Leclaire, A. Parmigiani, O. Malaspinas, B. Chopard, and J. Latt, Generalized three-dimensional lattice boltzmann color-gradient method for immiscible two-phase pore-scale imbibition and drainage in porous media, Phys. Rev. E 95, 033306 (2017).

[39] I. Ispolatov and M. Grant, Lattice boltzmann method for viscoelastic fluids, Phys. Rev. E 65, 056704 (2002).

[40] M. Yoshino, Y. Toriumi, and M. Arai, Lattice boltzmann simulation of two-phase viscoelastic fluid flows, J. Comput. Sci. Technol. 2, 330 (2008).

[41] Z. Guo, C. Zheng, and B. Shi, Force imbalance in lattice boltzmann equation for two-phase flows, Phys. Rev. E 83, 036707 (2011).

[42] Z. Guo, C. Zheng, and B. Shi, Non-equilibrium extrapolation method for velocity and pressure boundary conditions in the lattice boltzmann method, Chin. Phys. 11, 366 (2002).

[43] Q. Lou, Z. Guo, and B. Shi, Evaluation of outflow boundary conditions for two-phase lattice boltzmann equation, Phys. Rev. E 87, 063301 (2013).

[44] A. Satter and G. M. Iqbal, 3 - reservoir rock properties, in *Reservoir Engineering*, edited by A. Satter and G. M. Iqbal (Gulf Professional Publishing, Boston, 2016), pp. 29–79.

[45] See Supplemental Material at http://link.aps.org/supplemental/10.1103/PhysRevFluids.5.063301 for dynamic videos of the oil droplet displacements.

[46] Y. J. Liu, T. Y. Liao, and D. D. Joseph, A two-dimensional cusp at the trailing edge of an air bubble rising in a viscoelastic liquid, J. Fluid Mech. 304, 321 (1995).

[47] S. B. Pillapakkam, P. Singh, D. Blackmore, and N. Aubry, Transient and steady state of a rising bubble in a viscoelastic fluid, J. Fluid Mech. 589, 215 (2007).

[48] S. L. Ortiz, J. S. Lee, B. Figueroa-Espinoza, and B. Mena, An experimental note on the deformation and breakup of viscoelastic droplets rising in non-newtonian fluids, Rheol. Acta 55, 879 (2016).

[49] D. Fraggedakis, M. Pavlidis, Y. Dimakopoulos, and J. Tsamopoulos, On the velocity discontinuity at a critical volume of a bubble rising in a viscoelastic fluid, J. Fluid Mech. 789, 310 (2016).